Nanoscale

Accepted Manuscript

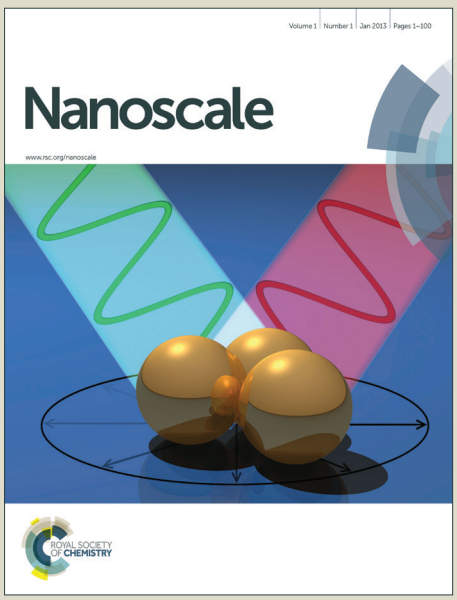

ROYAL SOCIETY OF CHEMISTRY

www.rsc.org/nanoscale

Nanoscale

ARTICLE

Synthesis of sub-nanosized Pt particles on mesoporous SBA-15 material and its application to the CO oxidation reaction

Received 00th January 20xx,
Accepted 00th January 20xx

DOI: 10.1039/x0xx00000x

www.rsc.org/

Hung-Chi Wu,[a] Tse-Ching Chen,[b] Nien-Chu Lai,[c] Chia-Min Yang,[c] Jia-Huang Wu,[a] Yan-Chu Chen,[a] Jyh-Fu Lee,[d] Ching-Shiun Chen[a,*]

In this work, we show that the size and shape of Pt nanoparticles in SBA-15 can be controlled through vacuum and air calcinations. The vacuum-calcination/H_2-reduction process is used to thermally treat a 0.2 wt% Pt^{4+}/SBA-15 sample to obtain small 2D clusters and single atoms that can significantly increase Pt dispersion in SBA-15. Compared with thermal treatments involving air-calcination/H_2-reduction, which result in ~ 4.6 nm rod-like Pt particles, vacuum-calcination/H_2-reduction can dramatically reduce the size of the Pt species to approximately 0.5–0.8 nm. The Pt particles undergoing air-calcination/H_2-reduction have poor conversion efficiency because the fraction of terrace sites, the major sites for CO oxidation, on the rod-like Pt particles is small. In contrast, a large amount of low-coordinated Pt sites associated with 2D Pt species and single Pt atoms in SBA-15 is effectively generated through the vacuum-calcination/H_2-reduction process, which may facilitate CO adsorption and induce strong reactivity toward CO oxidation. We investigated the effect of vacuum-calcination/H_2-reduction on the formation of tiny 2D clusters and single atoms by characterizing the particles, elucidating the mechanism of formation, determining the active sites for CO oxidation and measuring the heat of CO adsorption.

1. Introduction

Platinum catalysts have been widely used in industrial applications, including the reduction of pollutant gases in the environment, electrocatalytic reaction, hydrogenation and complete oxidation.[1–13] The catalytic oxidation of carbon monoxide to carbon dioxide is an essential reaction for environmental protection because of its importance in emission control.[14–20] Pt is recognized as a scarce resource and a limiting step in the development with high levels of catalytic activity because of the high cost of this precious metal. Thus, enhancement of the efficiency of these Pt catalysts is an attractive topic in catalysis research. The preparation of small metallic Pt nanoparticles (NPs) has been extensively investigated and is viewed as an active area of research in solid-state physics and chemistry. In comparison to the bulk material, platinum NPs typically offer increased concentrations of partially coordinated surface sites and consequently appear to be highly reactive in catalytic reactions. Recently, the shape- and size-controlled syntheses of Pt NPs have become an attractive goal for the development of catalysts with increased fractions of low-coordinated Pt surface atoms.[21–26] Alternatively, single-atom catalysts on Pt_1/FeO_x and Pt_1/Al_2O_3 supports could be developed and used in the CO oxidation reaction because the Pt loading of these catalysts has been reduced to as low as ~0.2 wt%.[19,20]

In recent years, mesoporous silica materials, e.g., MCM-41, MCM-48 and SBA-15, have been used extensively as catalyst supports because they possess high surface areas.[27–31] In the preparation of Pt NPs, SBA-15 mesoporous materials are frequently used to improve Pt dispersion, obtain nanosized Pt particles and control the shape of Pt particles because of their high surface area and ordered structure.[1] The synthesis of highly dispersed Pt catalysts may enhance the efficiency of catalytic reactions while reducing the use of Pt metal.

In general, thermal treatments performed by calcination in air and reduction in H_2 can lead to the formation of 3D Pt NPs. When SBA-15 is used as a support, the growth of Pt NPs usually occurs along the direction of the channel, which results in the formation of nanowire or nanorod shapes.[25] However, tiny Pt clusters less than 1 nm and/or single Pt atoms are usually difficult to generate in SBA-15 channels through traditional thermal treatments with air-calcination and H_2-reduction, even if a low Pt loading is used.[32,33] In this investigation, an as-impregnated Pt^{4+}/SBA-15 sample calcined under vacuum is used to generate large amount of tiny Pt clusters and single Pt atoms in SBA-15 materials. The catalytic activity of the CO oxidation reaction was compared for Pt species subjected to different calcination processes (i.e., air- and vacuum-calcination). We used a variety of experimental techniques to characterize the Pt NPs, probe their mechanism

[a] Center for General Education, Chang Gung University, 259, Wen-Hua 1st Rd., Guishan Dist., Taoyuan City 333, Taiwan, Republic of China.
[b] Department of Pathology, Chang Gung Memorial Hospital, 5 Fusing St., Guishan Dist., Taoyuan City 333, Taiwan, Republic of China.
[c] Department of Chemistry, National Tsing Hua University, Hsinchu 300, Taiwan, Republic of China.
[d] National Synchrotron Radiation Research Center, Hsinchu 300, Taiwan, Republic of China.
* E-mail of Corresponding Author: cschen@mail.cgu.edu.tw

of formation and investigate the catalytic behavior of Pt sites for CO oxidation.

2. Experimental

2.1 Catalyst preparation

Mesoporous SBA-15 silica was synthesized by adding 40.2 g of tetraethoxysilane (TEOS) to a pre-mixed solution of 10.8 g of 35% HCl solution and 18.7 g of pluronic P-123 ($EO_{20}PO_{70}EO_{20}$), which yielded a mixture with a molar composition of 1 TEOS:0.017 P-123:0.54 HCl:100 H_2O. The mixture was stirred at 308 K for 24 h and further aged at 363 K for 24 h. The product was filtered and dried at 363 K. The as-synthesized SBA-15 was calcined at 813 K for 6 h to remove the copolymer template. The Pt/SBA-15 catalyst was prepared by impregnating 1 g of the SBA-15 sample with 20 mL of 5.1×10^{-4} M aqueous H_2PtCl_6 to prepare 0.2 wt% Pt catalysts. The Pt/SBA-15-VH sample was obtained by vacuum-calcination of the impregnated Pt^{4+}/SBA-15 under vacuum (4×10^{-5} torr) at 673 K for 5 h and subsequent reduction under H_2 at 673 K for 5 h. In the case of the impregnated Pt^{4+}/SBA-15 calcined in air and reduced in H_2 at 673 K for 5 h, the sample is denoted as Pt/SBA-15-AH.

2.2 Brunauer–Emmett–Teller (BET) surface area measurements

N_2 physisorption isotherms were measured at 77 K using a Quantachrome Autosorb-1-MP instrument. Brunauer–Emmett–Teller (BET) surface areas were calculated from the adsorption branches in the relative pressure range of 0.05–0.30. The isotherms were analyzed by the nonlocal density functional theory (NLDFT) method to evaluate the pore sizes of the samples using the kernel of NLDFT equilibrium capillary condensation isotherms of nitrogen at 77 K on silica (adsorption branch assuming cylindrical pore geometry); the total pore volumes were evaluated at a relative pressure of 0.95.

2.3 Small- and wide-angle X-ray diffraction (XRD) measurements

The structures of the SBA-15 before and after Pt deposition were identified by small-angle X-ray diffraction (XRD) patterns recorded on a MacScience MXP18AHF diffractometer equipped with a Cu K_α radiation source (0.1549 nm). The Pt in the Pt/SBA-15 samples was characterized by wide-angle XRD patterns collected over the 2θ range from 20 to 70^o on a Rigaku Miniflex II equipped with a Cu K_α radiation source (0.1549 nm).

2.4 Transmission electron microscopy (TEM)

High-resolution TEM analyses were performed on a JEOL-JEM3000F instrument located at the High Valued Instrument Center of the National Tsing Hua University, Taiwan. The instrument was operated at 300 KeV. After the catalyst samples were pre-treated, they were dispersed in methanol and the resulting solution was ultrasonically mixed at room temperature. A portion of this solution was dropped onto a Cu grid for TEM imaging.

2.5 In situ X-ray absorption spectroscopy (XAS)

XAS spectra were recorded at the BL17C1 beam line at the National Synchrotron Radiation Research Center (NSRRC), Taiwan; the electron storage ring was operated at 1.5 GeV. All the XAS powder studies of the NPs were conducted in a custom stainless steel cell. Two holes were made in the cell, one on the top of the cell and the other on one side. After the solid samples were placed inside the cell, the holes were closed with Kapton film to avoid exposure of the sample to the ambient atmosphere. All spectra were recorded at room temperature in transmission mode. The higher harmonics were eliminated via detuning of the double Si(111) crystal monochromator. Three gas-filled ionization chambers were used in series to measure the intensities of the incident beam (I_0), the beam transmitted by the sample (I_t) and the beam subsequently transmitted by the reference foil (I_r). The third ion chamber was used in conjunction with a Pt foil reference sample for Pt L_3-edge measurements. The parameters for the extended X-ray absorption fine structure (EXAFS) measurements, data collection modes and error calculations were all controlled according to the guidelines set by the International XAFS Society Standards and Criteria Committee. The EXAFS data were reduced using standard procedures. We obtained the EXAFS function χ by subtracting the post-edge background from the overall absorption and normalizing with respect to the edge jump step. The normalized $\chi(E)$ was transformed from energy space to k-space, where k is the photoelectron wave vector. The $\chi(k)$ data were multiplied by k^3 for the Pt L_3-edge experiments to compensate for the dampening of the EXAFS oscillations in the high k region. Subsequently, the $\chi(k)$ data in k-space, which ranged from 3.1 to 12.4 $Å^{-1}$ for the Pt L_3-edge, were Fourier transformed (FT) to r-space to separate the EXAFS contributions of the different coordination shells. All computer programs were implemented using the UWXAFS 3.0 software package, and the backscattering amplitude and the phase shift for the specific atom pairs were theoretically calculated using the FEFF7 code. Structural parameters such as the coordination number (N) and the bond distance (R) were successfully calculated from these analyses.

2.6 Measurement of the FT-IR spectra

The in situ DRIFT analysis of CO adsorption was performed using a Nicolet 5700 FTIR spectrometer equipped with a mercury cadmium telluride (MCT) detector; the instrument was operated at 1 cm^{-1} resolution, 2.6 Measurement of the FT-IR spectra The in situ DRIFT analysis of CO adsorption was performed using a Nicolet 5700 FTIR spectrometer equipped with a mercury cadmium telluride (MCT) detector; the instrument was operated at 1 cm^{-1} resolution, and 256 scans were collected. The DRIFT cell (Harrick) was equipped with ZnSe windows and with a heating cartridge that allowed the sample to be heated to 773 K. Samples used to obtain IR spectra of CO adsorbed onto Pt/SBA-15 were prepared by passing CO through Pt/SBA-15 samples for 30 min at room

Table 1 Characterization of Pt/SBA-15 catalysts

Catalyst	CO adsorption (μmol/g cat.)	Pt surface area[a] (m^2/g)	Pt particle size[b] (nm)	Dispersion (%)
Pt/SBA-15-VH	7.4	0.62	nd[c]	72
Pt/SBA-15-AH	2.8	0.24	4.6	28

[a]Estimate from CO chemisorption; [b]Estimate from the XRD spectra in Fig. 1; [c]The XRD pattern was too weak to be observed.

temperature; the residual gaseous CO was purged using a He stream for 60 min.

2.7 Measurement of the Pt surface area

The Pt surface areas of the Pt/SBA-15 catalysts were measured via saturated CO chemisorption at room temperature in a glass vacuum system. All Pt catalysts were calcined in air and reduced under H_2 at 673 K for 5 h before CO chemisorption. The Pt sample disk was prepared by pressing 0.2 g of catalyst at 260 atm; the disk was repeatedly reduced under 760 torr H_2 at 673 K for 2 h and then heated under vacuum at 4×10^{-5} torr and at 673 K in a glass vacuum system for 30 min. Twenty torr of CO was introduced to the catalyst at room temperature for 10 min to achieve uptake saturation. The surface area of the Pt catalyst was calculated assuming a stoichiometric CO/Pt ratio of 1. The average surface density of the Pt metal was 7.1×10^{18} Pt atoms/m^2.[34]

2.8 Catalytic tests for CO oxidation

All CO oxidation reactions were performed in a fixed-bed reactor (0.95 cm inner diameter) at atmospheric pressure. A thermocouple connected to a PID temperature controller was placed on top of the catalyst bed. The CO oxidation activity measurements were performed in a fixed-bed reactor at atmospheric pressure. The gas reactant mixture containing 4.5% CO and 2.23% O_2 was passed through the catalyst bed. All products were analyzed via gas chromatography (GC) through a 12-ft Porapak-Q column; the gas chromatograph was equipped with a thermal conductivity detector (TCD).

3. Results

3.1 XRD spectra and CO chemisorption of Pt/SBA-15

Fig. 1 shows the XRD patterns of the reduced Pt structures on SBA-15; the patterns exhibit peaks at $2\theta = 39.6^o$, 46.0^o and 67.2^o; these peaks correspond to the (111), (200) and (220) facets, respectively. The average particle size of the reduced Pt/SBA-15 samples was calculated according to the Scherrer equation using the full-width at half-maximum (fwhm) values of the Pt(111) peaks, as shown in Table 1. The Pt surface area and dispersion of all the Pt/SBA-15 catalysts used in the experiments were measured via saturated CO chemisorption at room temperature. The size of the Pt NPs of the Pt/SBA-15-AH sample estimated from the XRD pattern was ~4.6 nm, and the CO chemisorption results indicated 28% Pt dispersion. When the impregnated Pt^{4+}/SBA-15 sample was subjected to vacuum calcination followed by reduction under H_2, the XRD signal of Pt/SBA-15-VH was too weak to be discriminated from the background. The Pt surface area and dispersion of Pt/SBA-15-VH were ca. 2.6 times greater than the surface area and dispersion of the Pt/SBA-15-AH sample; this increase is ascribed to the effect of vacuum calcination on the Pt/SBA-15-VH.

3.2 TEM images

HRTEM images of the reduced Pt/SBA-15 catalysts are shown in Fig. 2. The Pt particles apparently formed inside the channels of SBA-15. In the image of the reduced 0.2 wt% Pt/SBA-15-VH sample (image a), extremely tiny Pt particles less than 1 nm in diameter were observed to be dispersed in the SBA-15 structure. This observation suggests a reasonable interpretation of why the XRD pattern of the 0.2 wt% Pt/SBA-15-VH sample exhibit no discernible peaks (Fig. 1). In the case of the 0.2 wt% Pt^{4+} impregnated onto SBA-15 via air-calcination and H_2-reduction (Pt/SBA-15-AH), large Pt NPs confined in the structure SBA-15 were clearly observed (images b and c). Several spheroidal Pt NPs formed inside the channels of the pure SBA-15 structure.

3.3 Small-angle XRD and BET results

Fig. 3 shows the small-angle XRD patterns of the SBA-15 support with and without the reduced Pt nanoparticles. Each spectrum exhibited three well-resolved diffraction peaks in the region of $2\theta=0.5–2.0^o$; these peaks were indexed to the (100), (110), and (200) planes characteristic of a material with 2D

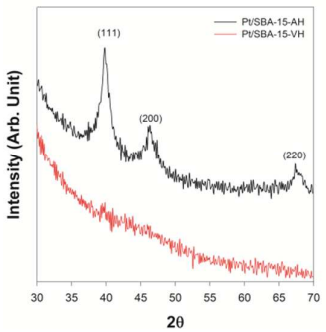

Fig. 1 XRD spectra of Pt/SBA-VH and Pt/SBA-15-AH catalysts.

Table 2. Textural properties of SBA-15, 0.2 wt% Pt/SBA-15-AH and 0.2 wt% Pt/SBA-15-VH

Sample	2θ	d_{100} (nm)	a_0 (nm)	D_{DFT} (nm)	S_{BET} ($m^2 g^{-1}$)	V_t ($cm^3 g^{-1}$)	V_m ($cm^3 g^{-1}$)
SBA-15	1.1	8.2	9.4	5.9	597	0.67	0.049
0.2 wt% Pt/SBA-15-AH	1.1	8.2	9.4	5.9	535	0.61	0.042
0.2 wt% Pt/SBA-15-VH	1.1	8.2	9.4	5.9	551	0.61	0.018

a_0: unit cell parameter; D_{DFT}: mesopore diameter; S_{BET}: BET surface area; V_t: total pore volume; V_m: micropore volume.

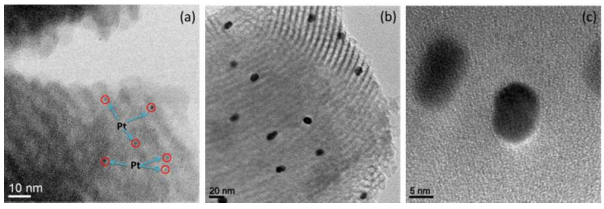

Fig. 2 HRTEM images of (a) 0.2 wt% Pt/SBA-15-VH and (b) and (c) 0.2 wt% Pt/SBA-15-AH.

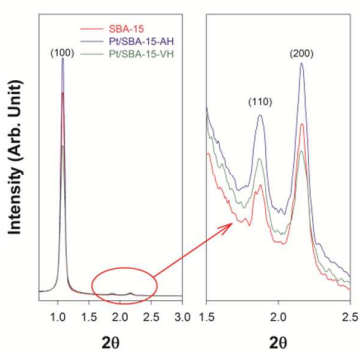

Fig. 3 Small-angle XRD patterns of the SBA-15 and Pt/SBA-15 samples.

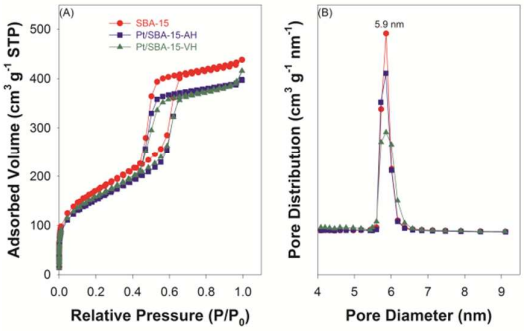

Fig. 4 (A) N_2 adsorption–desorption measurements and (B) pore size distributions of the SBA-15 and Pt/SBA-15 samples.

hexagonal symmetry. The formation of Pt NPs in Pt/SBA-15-AH and Pt/SBA-15-VH did not appear to induce a shift in the diffraction peaks relative to the peaks of the SBA-15 support because of the low 0.2 wt% Pt loading used in these cases.

The textural properties of the mesoporous materials both with and without Pt particles were examined using N_2 physisorption measurements (Fig. 4A). The textural properties obtained from the N_2 physisorption measurements are summarized in Table 2. All the samples exhibited type IV adsorption isotherms. A hysteresis loop with a sloping adsorption branch and a relatively sharp, steep desorption branch was observed at the relative pressure (P/P_0). The presence of a H1-type hysteresis loop suggests that the mesoporous channels remained cylindrical after the deposition of Pt particles. The pore size distributions of the samples, which were calculated from the N_2 adsorption isotherms using the kernel of the nonlocal density functional theory (NLDFT) equilibrium capillary condensation isotherms of nitrogen at 77 K on silica (adsorption branch, assuming cylindrical pore geometry), are presented in Fig. 4B. The average pore sizes of the SBA-15, Pt/SBA-15-AH and Pt/SBA-15-VH were centered at ~5.9 nm, which is consistent with the observation of the small angle XRD patterns. The deposition of Pt NPs in the SBA-15 support might decrease the accessible pore volume and surface area, but it did not influence the structure of SBA-15. The micropore volume (V_m) for the SBA-15 with and without Pt NPs were also measured and compared in Table 2. The V_m of Pt/SBA-15-AH was slightly lower than that of pure SBA-15. Interestingly, the formation of Pt NPs in the Pt/SBA-15-VH sample apparently led to a low V_m value.

3.4 X-ray absorption spectroscopy (XAS)

Fig. 5 shows the L_3-edge X-ray absorption near edge structure (XANES) spectra of the Pt; these spectra were collected while the Pt/SBA-15 was being subjected to various pretreatments. The white line representing the resonance peak at the absorption edge is attributed to the electron transition from $2p_{3/2}$ to $5d_{5/2}$ and $5d_{3/2}$.[2–4,35,36] The intensity of the white line at the L_3 edge indicates the electronic state of the absorbing atoms. A more intense white line implies greater electron vacancy in the d-orbitals.[2–4,35,36] In Fig. 5A, the white lines for the Pt NPs of Pt/SBA-15-VH after reduction at 673 K for 5 h are slightly more intense than those for the Pt foil standard, implying that a weakly positive charge ($Pt^{\delta+}$) may have been present. In the case of the Pt/SBA-15-AH sample, the intensity of the white line for the Pt^{4+}-impregnated SBA-15 decreased with continued calcination and reduction pretreatments, which, on the basis of a comparison to the spectrum of Pt foil, indicates the transformation of Pt^{4+} to Pt^0 (Fig. 5B). The XANES

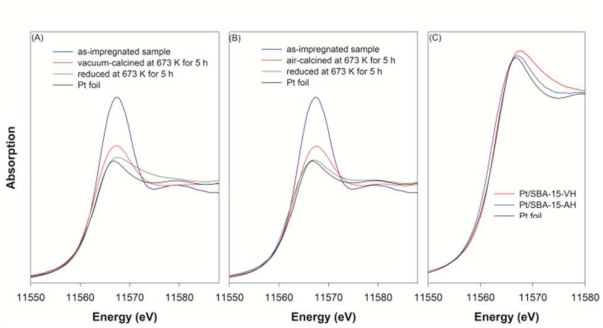

Fig. 5 Pt L_3-edge XANES spectra of the impregnated, calcined and reduced Pt samples of (A) 0.2 wt% Pt/SBA-15-VH; (B) 0.2 wt% Pt/SBA-15-AH; and (C) reduced Pt/SBA-15-VH, Pt/SBA-15-AH and Pt foil.

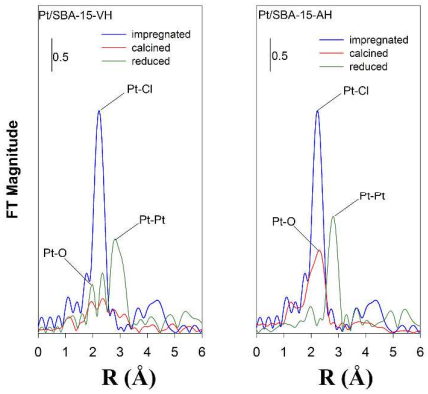

Fig. 6 Fourier-transformed EXAFS spectra for the impregnated, calcined and reduced Pt samples of 0.2 wt% Pt/SBA-15-VH and 0.2 wt% Pt/SBA-15-AH.

spectra obtained for both the reduced Pt/SBA-15-AH and Pt/SBA-15-VH samples were of size and shape on these Pt NPs in SBA-15 could be investigated via the Pt L_3-edge XANES spectra. Literatures have reported that the XANES spectra for sub 3-nm Pt NPs prepared by H_2 chemisorption show an increase in the width of the absorption peak and a shift in the absorption peak to higher energy with decreasing size of the Pt NPs.[37–40] In this case, the XANES peak (white line, WL) of Pt/SBA-15-VH was broader and shifted to a higher energy compared to those of the Pt/SBA-15-AH and the bulk Pt reference, as shown in Fig. 5C, suggesting that the Pt/SBA-15-VH sample may contain very small Pt NPs. As expected, compared to the XANES spectrum of the Pt foil reference material, no drastic change was observed in the spectral features and small energy shift was observed in the XANES spectra of the Pt/SBA-15-AH containing ~4.6 nm Pt NPs. A combination of in situ XANES spectroscopy and density functional theory (DFT) calculations was used to measure morphological changes and the particle size of Pt NPs under hydrogen environments. An energy shift of the WL peak greater than +1.0 eV relative to the corresponding peak of the Pt foil was observed to be more likely for NPs with a 2D-biplanar shape smaller than 1 nm. In contrast, the NPs tended to form a 3D shape as the size of the NPs increased, with the energy shift of the WL peak decreasing. In this study, the blue shifts of the WL for Pt NPs were ~1.02 eV for Pt/SBA-15-VH and 0.45 eV for Pt/SBA-15-AH, indicating that the Pt NPs likely formed 2D- and 3D-like structures for Pt/SBA-15-VH and Pt/SBA-15-AH, respectively.

The local structures of the Pt atoms in both Pt/SBA-15 catalysts were investigated via L_3-edge extended X-ray absorption fine structure (EXAFS). The Fourier transforms of k^3-weighted EXAFS results at the Pt L_3-edge with phase correlation for the impregnated, calcined and reduced Pt loaded onto SBA-15 support are shown in Fig. 6. The $k^3\chi(k)$ spectra were obtained through a comparison of the FEFF theoretical fit with the back-transformed experimental EXAFS data. The structural parameters extracted from the best-fit EXAFS data for the calcined and reduced Pt samples are listed in Table 3. The Pt^{4+}/SBA-15 sample calcined in air was assumed to have generated typical Pt oxides that led to Pt–O bonding with a coordination number, N_{Pt-O}, of approximately 5.3 and a Pt–O distance of 2.12 Å. The Pt–Pt bonding data could not be effectively analyzed from the EXAFS spectra. The Pt oxides on the SBA-15 became more metallic, with a coordination number N_{Pt-Pt} of 10.7 and Pt–Pt bond distance of 2.75 Å, as the reduction at 673 K progressed. The Fourier transforms of the

Table 3 Structural parameters of 0.2 wt% Pt/SBA-15-AH and 0.2 wt% Pt/SBA-15-VH

Pretreatment	Shell	N	R (Å)	r^a ($\times10^{-2}$)	σ^2 ($Å^2$)^b	ΔE_0 (eV)^c
Impregnation	Pt-Cl	4.8	2.32	0.85	0.0019	10.0
Air calcination	Pt-O	5.3	2.12	0.17	0.0094	17.0
Reduction (Pt/SBA-15-AH)	Pt-Pt	10.7	2.75	0.33	0.0063	6.3
Vacuum calcination	Pt-O	1.6	1.95	0.54	0.0063	-1.7
	Pt-Cl	1.1	2.32	0.54	0.0049	13.6
	Pt-Pt	0.9	2.81	0.54	0.0035	18.4
Reduction (Pt/SBA-15-VH)	Pt-Pt	6.8	2.76	0.70	0.0046	8.25
	Pt-O	0.3	2.01	0.70	0.0004	6.54

[a]Residual factor; [b]Debye—Waller factor, [c]The inner potential correction

Journal Name

ARTICLE

EXAFS data for the Pt^{4+}/SBA-15 sample treated by vacuum-calcination at 673 K for 5 h revealed insignificant peaks.
Analysis of the EXAFS indicated Pt–O, Pt–Cl, and Pt–Pt bond lengths of 1.95 Å, 2.32 Å and 2.81 Å, respectively. Low coordination numbers of 1.6, 1.1 and 0.9 were obtained for the Pt–O, Pt–Cl and Pt–Pt bonding, respectively. When the vacuum-calcined Pt/SBA-15 sample was further reduced in H_2, the Pt–Pt contribution at a distance of 2.76 Å with an average coordination number of 6.8 and the weak Pt–O binding with a coordination number of 0.3 at a distance of 2.01 Å were observed.

3.5 IR spectra of CO adsorbed onto Pt/SBA-15

We used CO as a probe molecule to identify the active sites on the reduced Pt catalysts because of the utility of CO in vibrational spectroscopy, which can provide information related to the surface sites of an adsorbed species and to the chemical environment of a Pt surface. The difference among the CO molecules adsorbed onto the reduced Pt/SBA-15 via different calcination treatments was specifically examined in this work. Fig. 7 shows the IR spectra of the CO adsorbed on both of the Pt/SBA-15 catalysts at room temperature. The vibrational frequency of the IR bands at frequencies greater than 2000 cm^{-1} was assigned to linear CO adsorption onto the Pt surfaces. The CO chemisorption onto both Pt surfaces resulted in a large difference in intensity in the corresponding IR spectra. The weak and broad IR band of the CO adsorbed onto reduced Pt/SBA-15-AH was fitted using three principle peaks at 2053 cm^{-1} (L_1 state), 2070 cm^{-1} (L_2 state) and 2086 cm^{-1} (L_3 state). Three types of sites for CO adsorption are likely present on the surface of reduced Pt/SBA-15-AH. However, CO adsorbed onto the reduced Pt/SBA-15-VH gave an intense and symmetrical IR peak centered at 2076 cm^{-1}. The band width of the IR peak for Pt/SBA-15-VH was narrower than that for Pt/SBA-15-AH, implying that uniform, small Pt particles were likely formed in the Pt/SBA-15-VH sample.
Fig. 8 reveals the IR spectra of equilibrium CO adsorbed onto the reduced Pt/SBA-15 catalysts at different adsorption temperatures. The intensity of the IR peaks of CO adsorbed onto the reduced Pt/SBA-15-VH gradually decreased with increasing adsorption temperature; however, an intense peak of CO adsorbed onto the Pt surface was observed even in the case of CO adsorption conducted at 673 K, as shown in Fig. 8A. The vibrational frequency of the adsorbed CO exhibited a red-shift from 2076 cm^{-1} to 2060 cm^{-1} with decreasing CO coverage on the reduced Pt/SBA-15-VH. This behavior is very characteristic of CO linearly adsorbed onto a Pt surface and is usually explained by dipole-dipole interactions. The temperature dependence of the IR spectra of equilibrium CO adsorbed onto reduced Pt/SBA-15-AH is shown in Fig. 8B. The weak IR peak vanished until 423 K and then remained at a similar intensity at temperature greater than 473 K.
On the basis of the aforementioned IR results, Pt/SBA-15-VH apparently exhibits a surprisingly ability to adsorb CO molecules. Thus, the adsorption equilibrium-infrared spectroscopy (AEIR) method was used to determine the heats of adsorption of the CO species onto both Pt/SBA-15 samples.[41-51] On the basis of the spectra in Fig. 8, the coverage of the CO species (θ) obtained in temperature-dependence studies of the equilibrium CO adsorbed onto the Pt/SBA-15 surfaces are displayed in Fig. 9. The CO coverage was

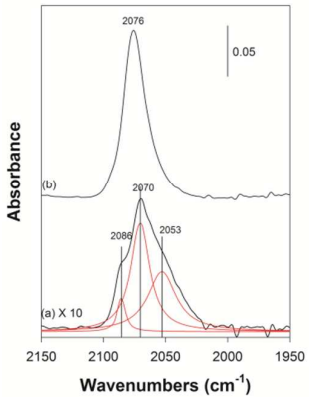

Fig. 7 IR spectra of CO adsorbed onto the reduced (a) 0.2 wt% Pt/SBA-15-AH and (b) 0.2 wt% Pt/SBA-15-VH.

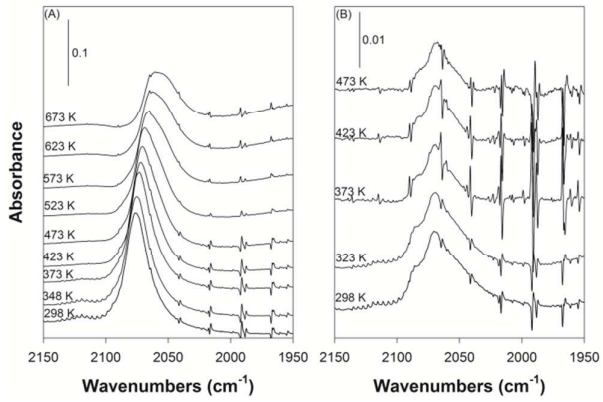

Fig. 8 IR spectra of equilibrium adsorption of CO adsorbed onto (A) reduced 0.2 wt% Pt/SBA-15-VH and (B) reduced 0.2 wt% Pt/SBA-15-AH at various adsorption temperatures. CO adsorptions were performed via exposure to a 20 mL/min pure CO stream at a constant pressure of P_{CO} = 101.3 kPa for 30 min, followed by a 20 mL/min helium stream for 50 min at the desired temperature to purge the CO gas.

determined using the ratio A/A_0, where A is the IR band area at different temperatures and A_0 is the initial IR band area of saturated adsorption at 298 K. The experimental curves in Fig. 9 are suggested to correspond to the Temkin model, where the values of adsorption heat (E_0) linearly decrease with the coverage θ ($E_0=E_0-\alpha\theta$).[41-51] This equation leads to the generalized expression of the coverage as a function of the adsorption parameter:

$$\theta = \frac{RT_a}{\Delta E}\ln\left(\frac{1+K_0P_a}{1+K_1P_a}\right) \quad (1)$$

where $\Delta E=E_0-E_1$ is the difference in the adsorption heat between very small coverage (E_0) and saturation coverage (E_1) and K_0 and K_1 are the adsorption coefficients at $\theta=0$ and $\theta=1$, respectively. According to the Temkin model, we can assume $K_0P_a >> 1$ and $K_1P_a<<1$ and the adsorption coefficients at $\theta=0$ can be expressed by

$$K_0 = Ae^{\frac{E_0}{RT_a}}$$

Thus, equation (1) becomes

$$\theta = \left[\frac{R}{E_0-E_1}\ln(AP_a)\right]T_a + \frac{E_0}{E_0-E_1} \quad (2)$$

Equation (2) corresponds to the linear fraction of the curves in Fig. 9, and the extension of the linear section leads to the θ-axis intercept with a value of E_0/E_0-E_1.

The adsorption coefficients can be derived using statistical thermodynamics under the assumption of non-activated and localized CO adsorption, as follows:

$$K_0 = \frac{h^3}{k(2\pi mk)^{3/2}}\frac{1}{T_a^{5/2}}e^{\frac{E_0}{RT_a}} = Ae^{\frac{E_0}{RT_a}} \quad (3)$$

where h is Planck's constant, k is Boltzmann's constant, and E represents the CO adsorption energy. Equation (3) yielded a pre-exponential factor, A, of 1.7×10^{-12} Pa^{-1} at 300 K. The slopes of the straight lines in Fig. 9 gave values of ΔE=64.2 KJ/mol for Pt/SBA-15-VH and ΔE=21.6 KJ/mol for Pt/SBA-15-AH under the assumption that $A=1.7\times10^{-12}$ Pa^{-1}. The interception points of the straight lines in Fig. 9A and 9B represent the values of $E_0/\Delta E$ for CO adsorbed onto both Pt/SBA-15 samples, leading to E_0=120.0 and E_1=55.8 KJ/mol for CO adsorption onto Pt/SBA-15-VH and to E_0=60.6 and E_1=39 KJ/mol for CO adsorption onto Pt/SBA-15-AH. The adsorption heat of CO adsorbed onto Pt/SBA-15-VH was obviously higher than that of CO adsorbed onto Pt/SBA-15-AH. This observation explains why the sites of Pt/SBA-15-VH exhibit stronger binding ability for CO compared to those of Pt/SBA-15-AH.

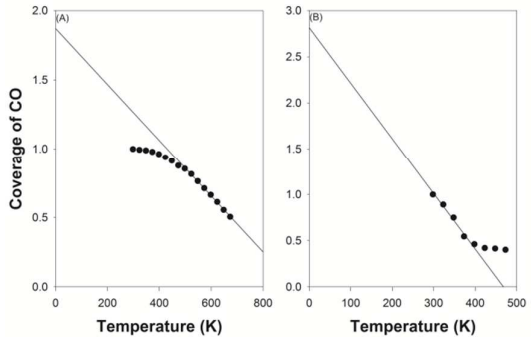

Fig. 9 Change in the coverage of CO species in equilibrium adsorption as a function of the adsorption temperature shown in Fig. 8 for (A) 0.2 wt% Pt/SBA-15-VH and (B) 0.2 wt% Pt/SBA-15-AH.

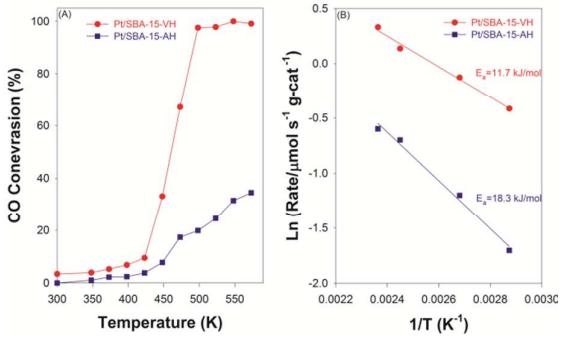

Fig. 10 Comparison of the conversion in CO oxidation between the 0.2 wt% Pt/SBA-15-VH and 0.2 wt% Pt/SBA-15-AH catalysts for (A) the temperature-dependent reactions and (B) Arrhenius plots.

3.6 Catalytic CO oxidation over Pt/SBA-15 catalysts

The temperature dependence of the CO conversion for both reduced Pt/SBA-15 catalysts is shown in Fig. 10A. The Pt/SBA-15-VH sample exhibited dramatically higher efficiency for CO oxidation compared to the Pt/SBA-15-AH sample. For the Pt/SBA-15-VH catalyst, 3.4–9.5% CO conversion was achieved in the temperature range from 300 to 423 K, with complete CO oxidation occurring at 498 K. The Arrhenius plots, which provide the apparent activation energies for CO oxidation on both reduced Pt/SBA-15 catalysts, are shown in Fig. 10B. The apparent activation energy was estimated to be 11.7 KJ/mol for Pt/SBA-15-VH and 18.3 KJ/mol for Pt/SBA-15-AH.

Fig. 11 shows the dependence of the CO oxidation reaction rate on the partial pressures of CO and O_2 at 423 K for the Pt/SBA-15-VH and Pt/SBA-15-AH catalysts, respectively. The apparent reaction orders for CO and O_2 were similar on the two Pt/SBA-15 catalysts, giving rate laws of

$r = kP_{CO}^{-1.3}P_{O_2}^{0.26}$ for Pt/SBA-15-VH and

$r = kP_{CO}^{-1.3}P_{O_2}^{0.39}$ for Pt/SBA-15-AH.

On the basis of the aforementioned findings, the characteristic of CO adsorption onto Pt/SBA-15 catalysts may reflect their

relative activity toward CO oxidation. Therefore, further investigations of the adsorption of CO and air onto both Pt/SBA-15 catalysts were conducted, as shown in Fig. 12. As shown in Fig. 12A, when an air stream was introduced to Pt/SBA-15-VH whose surface was saturated with adsorbed CO, the intensity of the peak at 2076 cm^{-1} decreased rapidly within 10 s and almost disappeared at 40 s. In contrast, the Pt/SBA-15-AH catalyst exhibited poor CO removal efficiency in air for the same experiment. The L_3-state CO with a peak at 2086 cm^{-1} could be rapidly oxidized by air; however, the L_1 (2070 cm^{-1}) and L_2 (2053 cm^{-1}) CO appeared to exhibit low reactivity with air.

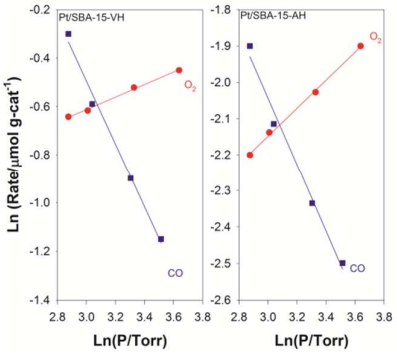

Fig. 11 Dependence of the reaction rate on the partial pressures of O_2 and CO for the 0.2 wt% Pt/SBA-15-VH and 0.2 wt% Pt/SBA-15-AH catalysts.

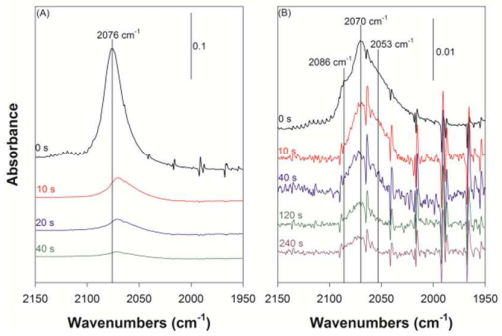

Fig. 12 Time dependence of the IR spectra for co-adsorption of CO and O_2 onto (A) 0.2 wt% Pt/SBA-15-VH and (B) 0.2 wt% Pt/SBA-15-AH at room temperature. All samples were exposed to a 30 mL/min pure CO stream at atmospheric pressure for 30 min, followed by a 30 mL/min helium stream to purge the CO gas for 30 min, after which an air stream was introduced into the reaction cell.

4. Discussion

4.1 Particle size and shape of the Pt species of Pt/SBA-15-AH and Pt/SBA-15-VH

The results of the present study show that calcination treatments in a vacuum environment and in an air stream at atmospheric pressure may induce large differences in the size of the Pt NPs and morphology of the Pt species of catalysts with a 0.2 wt% loading. In general, the shape of the Pt nanostructures formed might be associated with the difference in the growth rates between the {100} and {111} axes.[52] In our previous paper, we reported that Pt^{4+} ions could apparently aggregate to form long rod-like Pt NPs inside the SBA-15 channels through calcination in air at 673 K for 5 h.[25] However, the long spheroid-like Pt NPs of the Pt/SBA-15-AH sample in the channels of pure SBA-15 might follow the growth mechanism of nanorod structures in the course of H_2 reduction as a consequence of the ratio of the growth rates along the {100} and {111} axes being slightly less than 1.[25] The SBA-15 channels restricted the growth of Pt along the <100> direction and enhanced Pt NP aggregation along the <111> direction, which induced the formation of spheroid-like or rod-like Pt NPs.[52]

However, pretreatments associated with vacuum-calcination and subsequent H_2 reduction can induce a different morphology and growth mechanism for Pt NPs formation. In this study, effectively observing the shape and size of the tiny Pt NPs of Pt/SBA-15-VH in HRTEM images was difficult because the NPs were located inside the SBA-15 channels. However, XANES spectroscopy has been used to identify the morphology and electronic structure of subnanometer Pt NPs (~ 1 nm) with H_2 adsorption[37–40]. Under an H_2 environment, the interaction between H and the subnanometer Pt NPs can result in the geometrical relaxation of Pt–Pt bonding by H_2 and induce changes in the electronic structure of Pt.[37–40] Both effects can lead to an energy shift in the XANES absorption to greater than 1 eV, and this condition may influence the formation of the 2D NPs structure. The morphology of the large Pt NPs (> 3 nm) was likely a 3D structure; thus, no drastic changes in the XANES spectra were observed compared to the spectrum of bulk Pt. The WL peak of the Pt/SBA-15-VH sample reduced by H_2 adsorption was broader and significantly blue-shifted by ~1.02 eV relative to the corresponding peak of Pt foil, suggesting that the size of the Pt NPs in Pt/SBA-15-VH may be less than 1 nm and that the Pt NPs tend to form 2D structures (biplanar shape). In contrast, the Pt/SBA-15-VH exhibited high (72%) dispersion, implying that the sample may also contain extremely tiny Pt clusters and/or single atoms in the SBA-15 structure in addition to containing 2D NPs.

Analysis of the EXAFS results shows that the coordination number of Pt–Pt bonding was 6.3 for the reduced Pt/SBA-15-VH sample. Several studies have reported that the coordination numbers of Pt NPs obtained from EXAFS spectra can reflect their particle size. Mostafa *et al.* investigated the relationship between Pt NPs with average sizes of ~0.8–1.0 nm and coordination number and observed that the Pt coordination number was ca. 7.7 for 0.8 nm.[53] Molecular dynamics simulations have also been employed to estimate the first-shell Pt–Pt coordination number in nanoparticles with sizes ranging from 0.5 to 3.1 nm.[54] The Pt coordination number was ~5 for 0.5 nm and ~7 for 0.8 nm. Zhang and his co-workers have used HAADF-STEM images to observe 2D Pt NPs smaller than 0.8 nm formed on FeO_x.[55]On the basis of these previous studies, we can reasonably suggest that, in this case, the average size for 6.8-coordinate Pt is likely in the range from 0.5 to 0.8 nm. Undoubtedly, the generation of a 2D structure and single atoms should closely depend on impregnated Pt^{4+}/SBA-15 treated by vacuum-calcination. In our experience, thermal

treatment in H_2 for Pt NPs usually leads significant aggregation to form large particles. When the Pt^{4+}/SBA-15 sample was heated under vacuum, the original Pt–Cl coordination could convert to Pt–O, Pt–Cl or Pt–Pt bonding, giving a low coordination number with 1.6, 1.1 and 0.9, respectively (Table 3). The process of vacuum calcination may effectively disperse Pt atoms in the SBA-15 structure and then induce the formation of 2D Pt clusters and/or single atoms during the course of H_2 reduction. However, the formation of 2D Pt clusters and/or single atoms may result in strong interactions between Pt and SBA-15; consequently, slight Pt–O bonding was still observed after H_2 reduction.

The BET measurements in Table 2 show that the formation of 2D Pt clusters and single Pt atoms led to a significant reduction in the volume of the micropore in Pt/SBA-15-VH, indicating that these Pt species, including 2D Pt clusters and single Pt atoms, might be located primarily in the micropore structure. The structure of the SBA-15 support should consist of a 2D hexagonal array of cylindrical mesopores, a secondary pore network, and micropores.[56] The effect of SBA-15 micropores in the synthesis of metal particles has generally attracted little attention in the literature because the relevant information on the sizes and shapes of the micropores is difficult to obtain. Recently, the micropores in SBA-15 were directly measured to and were observed to exhibit a diameter between 0.57 and 0.62 nm.[55] As previously discussed above, the average size of Pt species in Pt/SBA-15-VH is estimated to be in the range from ~0.5 to ~0.8 nm. Thus, these Pt species, including 2D NPs and single atoms, might be confined in the micropore of SBA-15 and might cause a Pt–O interaction.

4.2 Active sites and CO adsorption for CO oxidation

The Pt/SBA-15-VH exhibited dramatically higher conversion efficiency for CO oxidation than the Pt/SBA-15-AH. The spheroid-like Pt NPs with a 3D structure in Pt/SBA-15-AH yielded poor conversion for CO oxidation. The 2D structure and single atoms may be the major morphologies of Pt NPs of Pt/SBA-15-VH after vacuum-calcination, which positively enhanced the efficiency of CO oxidation. In fact, in the case of the literature-reported shape-dependent catalytic oxidation of isopropanol on Pt NPs, 2D NPs exhibited better catalytic performance than 3D-shaped catalysts when NPs with analogous average sizes (0.8–1.0 nm) were compared.[53] Recently, single-atom catalysts of precious metals, such as Pt, Pd and Ir have attracted increasing attention for use in many catalytic reactions in attempts to achieve high levels of activity and reduce the use of noble metals.[19,20,55,57] Catalysts composed of single Pt atoms on Fe_2O_3 and Al_2O_3 for the CO oxidation, NO reduction and water-gas shift reactions have been reported in the literature; the supported single Pt atoms exhibited extremely high activity toward these reactions. A method of preparing single Pt atoms was also developed using the atomic layer deposition technique to enable the synthesis of a Pt/graphene catalyst.[58] The application of the single Pt atom catalyst in an electrocatalytic reaction resulted in excellent performance for methanol oxidation and superior CO tolerance. Single Ir atoms supported on FeO_x catalysts have also been developed as high activity catalysts for the water-gas shift reaction.[57] In addition, Ag-alloyed Pd single-atom catalysts exhibit excellent catalytic performance for the selective hydrogenation of acetylene.[59] The results of these previous studies suggest that very small and/or single-atom metal catalysts can positively enhance the catalytic efficiency in many reactions.

The significant difference in the morphology of Pt species in Pt/SBA-15-AH and Pt/SBA-15-VH may directly influence the chemical state of Pt species and the adsorption of the CO reactant. The results of XANES and EXAFS spectroscopy clearly indicated that tiny 2D Pt NPs or single Pt atoms of Pt/SBA-15-VH possess a slightly positive charge ($Pt^{\delta+}$) after reduction treatment, as indicated by the low coordination number for Pt–O bonding. Tiny 2D Pt NPs or single Pt atoms may be anchored in the micropore structure of SBA-15, leading to the weak contribution of Pt–O bonding from the possible interaction between Pt and the SBA-15 oxide support. Unlike Pt/SBA-15-VH, the large Pt NPs formed in the Pt/SBA-15-AH could not form in the micropore structure and were mainly distributed in the channel of the mesopore structure, so the Pt NPs could be completely reduced.

The chemical state of the Pt species has been hypothesized to be an important factor influencing the activity of supported Pt catalysts, where partially oxidized Pt atoms are expected to be highly active toward CO oxidation. The $Pt^{\delta+}$ species of Pt/SBA-15-VH associated with the presence of the metal-support interaction may also strongly affect the performance of the Pt catalyst in the present study. Assignments of the IR bands of CO adsorbed onto a Pt surface have been proposed in the literature.[60-65] The IR stretching frequency of CO adsorption has been interpreted in terms of the electronic and structural effects of Pt particles. According to the literature, the lower frequency bands at ~2075 and 2054 cm^{-1} in the IR spectra of CO adsorbed onto Pt surfaces correspond to CO on defect sites, such as edges and kinks.[60-65] The band located at 2096 cm^{-1} is assigned to CO adsorbed onto the close-packed terrace sites or oxidized $Pt^{\delta+}$ atoms.[65] The band at 2025 cm^{-1} is assigned to CO adsorbed onto Pt atoms of small particles.[65] Bazin *et al.* reported that the ν(CO) at ~2010 cm^{-1} might correspond to linear CO adsorbed onto very small Pt particles (< 1.5 nm) with low coordination and that the band at 2008 cm^{-1} is attributable to CO adsorbed onto Pt sites with very low coordination.[65]

According to calculations based on the XRD spectra, the reduced Pt/SBA-15-AH, which contains ca. 4.6 nm Pt NPs, may exhibit complicated CO adsorption sites, such as several flat surfaces and defect sites. Therefore, the lower frequency bands of the L_1 and L_2 CO on Pt/SBA-15-AH were most likely caused by CO binding to Pt atoms with low coordination or to imperfect Pt sites. The highest frequency band, which was observed at 2086 cm^{-1} for L_3 CO, might be ascribed to the CO adsorption onto the metallic terrace sites or oxidized $Pt^{\delta+}$ sites. However, the presence of oxidized $Pt^{\delta+}$ sites was very unlikely because the Pt particles of Pt/SBA-15-AH were completely reduced, as evidenced by analysis of the XANES and EXAFS spectra. The IR spectra of CO and air co-adsorbed onto Pt/SBA-15-AH (Fig. 12) indicated that the CO bound to terrace sites (L_3

CO) exhibits greater reactivity to form CO_2 compared to CO bound to the L_1 and L_2 sites when an air stream was introduced. In our previous study, we observed that CO adsorbed onto terrace sites was more easily oxidized to CO_2 compared to CO adsorbed onto other active sites.[25]

The adsorption sites on Pt/SBA-15-VH should mainly be 2D Pt NPs and single Pt atoms belonging to very low-coordinated Pt sites. Our previous study has reported that CO adsorbed on the defects of subnanosized Pt particles and/or single Pt atom might appear at the low ν(CO) with 2003 cm^{-1}.[66] However, it could give a likelihood of the ν(CO) shifted to higher frequency due to the tiny Pt cluster and/or Pt single atom weakly oxidized by support. Thus, we considered that the site for CO adsorption that gives the symmetrical IR band at 2076 cm^{-1} may be associated with the partial positive charge ($Pt^{\delta+}$). However, the $Pt^{\delta+}$ sites provided sufficiently high catalytic activity for CO oxidation that the adsorbed CO was rapidly oxidized by air at room temperature (Fig. 12). The $Pt^{\delta+}$ sites formed in Pt/SBA-15-VH due to the metal-support interaction might play an essential role in enhancing the ability of CO to be adsorbed onto the Pt surface.[18]

The AEIR procedure has been used to determine the adsorption heat of CO and provides useful information for characterizing surface sites on the Pt/SBA-15 catalysts. The values for E_0 and E_1 for CO adsorption onto Pt/SBA-15-VH were determined to be 120.0 and 55.8 KJ/mol using the Temkin model (Fig. 9A). The curve in Fig. 9B was obtained with E_0=60.6 and E_1=39 KJ/mol for CO adsorption onto Pt/SBA-15-AH. The small difference between E_0 and E_1 indicates that the Temkin model for CO adsorption on Pt/SBA-15-AH nearly corresponds to the Langmuir model. Undoubtedly, the significant energy differences in CO adsorbed onto both Pt/SBA-15 catalysts may reflect the different characterization of the Pt species. The adsorption heat of CO on Pt/SBA-15-VH was much higher than that on Pt/SBA-15-AH. This observation could explain why CO molecules can bind more strongly to Pt/SBA-15-VH than to Pt/SBA-15-AH. Notably, the large amount of CO strongly bound to the $Pt^{\delta+}$ sites of Pt/SBA-15-VH can be rapidly oxidized under an air stream, as shown in Fig. 8. In contrast, the Pt NPs of Pt/SBA-15-AH exhibited numerous types of active sites for CO adsorption but resulted in low CO coverage. Additionally, the number of terrace sites (L_3 CO) that contributed substantially to the reactivity was small; thus, poor catalytic efficiency for CO oxidation on Pt/SBA-15-AH catalyst was expected. On the basis of these results, the calcination treatment for impregnated Pt^{4+}/SBA-15 should be the key step for determining the dispersion and morphology of metallic Pt species.

From the kinetic results of CO oxidation on both Pt/SBA-15 catalysts, the reaction orders of O_2 and CO reactants gave positive and negative values, respectively, indicating that O_2 and CO molecules can competitively occupy the same sites. These results are in agreement with the literature that suggests that inhibition of the adsorption of O_2 by the strong binding of CO to Pt atoms may be the major reason why the reaction rate of CO oxidation is usually slow on Pt catalysts.[18,67] Because CO adsorption was stronger than O_2 adsorption on the Pt surface, the coverage of O_2 might be very small and exhibit little dependence on the partial pressure. A similar rate law for CO oxidation on both of the Pt/SBA-15 catalysts implies that the CO oxidation might undergo the same reaction mechanism on the Pt surfaces. The presence of 2D clusters and single atoms did not change the reaction behavior of CO oxidation on Pt. The major reason for the enhancement of CO oxidation on Pt/SBA-15-VH can be ascribed to the high dispersion of the Pt species, resulting in high CO coverage, thereby increasing the possibility of CO adsorption onto the surface reacting with O_2.

5. Conclusions

In this work, vacuum calcination was used to thermally treat 0.2 wt% Pt^{4+}/SBA-15 and effectively improve Pt dispersion in the SBA-15 structure. The thermal treatment with vacuum calcination and H_2 reduction of the 0.2 wt% Pt^{4+}/SBA-15 sample (Pt/SBA-15-VH) can significantly enhance the efficiency of CO oxidation compared to the 0.2 wt% Pt/SBA-15 prepared by air-calcination and H_2-reduction (Pt/SBA-15-AH). The large difference in the reactivity toward CO oxidation for both Pt/SBA-15 catalysts is assumed to be associated with the shape of the Pt species in SBA-15. In Pt/SBA-15-VH, the tiny 2D clusters and single atoms likely located in the micropore structure are the major Pt species, with an average particle size of 0.5–0.8 nm. The Pt sites associated with low coordination and sub-nanoscale 2D Pt NPs and/or single Pt atoms of Pt/SBA-15-VH containing a slightly positive charge are proposed as the major sites of CO oxidation; the character of these sites may facilitate CO adsorption and induce strong reactivity for CO oxidation. Vacuum-calcination can transform the original Pt–Cl species to highly dispersed Pt–Pt, Pt–O and Pt–Cl species, and the calcined Pt species can be subsequently reduced in H_2 to form tiny 2D clusters and single atoms. The effects of high CO coverage and partially oxidized Pt species on the Pt/SBA-15-VH catalyst significantly enhance CO oxidation. In the case of Pt/SBA-15-AH, air-calcination and H_2-reduction can cause the bonding of Pt species through the pathway Pt–Cl → Pt–O → Pt–Pt and form rod-like Pt NPs with an average particle size of ~4.6 nm in the SBA-15 channels. CO oxidation mainly occurs on the terrace sites on the large Pt NPs in the case of the 0.2 wt% Pt/SBA-15-AH but with poor conversion efficiency due to the small amount of active terrace sites on the surface.

Acknowledgements

Financial support from the Ministry of Science and Technology (MOST103-2113-M-182-001-MY3) and Chang-Gung Memorial Hospital (CMRPD5C0022) are gratefully acknowledged. We are also grateful for access to the in situ X-ray absorption spectroscopy (BL17C1) results collected at the National Synchrotron Radiation Research Center (NSRRC).

Notes and references

1 J. Zhu, T. Wang, X. Xu, P. Xiao and J. Li, *Appl. Catal. B*, 2013, **130–131**, 197–217.
2 Z. Jiang, Y. Yang, W. Shangguan and Z. Jiang, *J. Phys. Chem. C*, 2012, **116**, 19396–19404.
3 M. F. Williams, B. Fonfé, A. Jentys, C. Breitkopf, J. A. R. van Veen and J. A. Lercher, *J. Phys. Chem. C*, 2010, **114**, 14532–14541.
4 T. Ebashi, Y. Ishida, Y. Nakagawa, S. Ito, T. Kubota and K. Tomishige, *J. Phys. Chem. C*, 2010, **114**, 6518–6526.
5 J. Zhu, K. Kailasam, X. Xie, R. Schomaecker and A. Thomas, *Chem. Mater.*, 2011, **23**, 2062–2067.
6 V. T. T. Ho, C. J.Pan, J. Rick, W. N. Su and B. J. Hwang, *J. Am. Chem. Soc.*, 2011, **133**, 11716–11724.
7 Y. B. He, G. R. Li, Z. L. Wang, Y. N. Ou and Y. X. Tong, *J. Phys. Chem. C*, 2010, **114**, 19175–19181.
8 T. H. M. Housmans and M. T. M. Koper, *J. Phys. Chem. B*, 2003, **107**, 8557–8567.
9 M. Rodríguez-López, J. Solla-Gullón, E. Herrero, P. Tuñón, J. M. Feliu, A. Aldaz and Jr. Carrasquillo, *J. Am. Chem. Soc.*, 2010, **132**, 2233–2242.
10 S. W. Lee, S. Chen, W. Sheng, N. Yabuuchi, Y. T. Kim, T. Mitani, E. Vescovo and Y. Shao-Horn, *J. Am. Chem. Soc.*, 2009, **131**, 15669–15677.
11 C. Li, M. Imura and Y. Yamauchi, *Chem. Eur. J.*, 2014, **20**, 3277–3282.
12 C. Li, T. Sato and Y. Yamauchi, *Angew. Chem. Int. Ed.*, 2013, **52**, 8050–8053.
13 Y. J. Yamauchi, *Ceram. Soc. Jpn.*, 2013, **121**, 831–840.
14 Y. Jiao, H. Jiang and F. Chen, *ACS Catal.*, 2014, **4**, 2249–2257.
15 R. Ahmad and A. K. Singh, *ACS Catal.*, 2015, **5**, 1826–1932.
16 B. Qiao, A. Wang, L. Li, Q. Lin, H. Wei, J. Liu and T. Zhang, *ACS Catal.*, 2014, **4**, 2113–2117.
17 F. Li, Y. Li, X. C. Zeng and Z. Chen, *ACS Catal.*, 2015, **5**, 544–552.
18 N. An, S. Li, P. N. Duchesne, P. Wu, W. Zhang, J. F. Lee, S. Cheng, P. Zhang, M. Jia and W. Zhang, *J. Phys. Chem. C*, 2013, **117**, 21254–21262.
19 M. Moses-DeBusk, M. Yoon, L. F. Allard, D. R. Mullins, Z. Wu, X. Yang, G. Veith, G. M. Stocks and C. K. Narula, *J. Am. Chem. Soc.*, 2013, **135**, 12634–12645.
20 B. Qiao, A. Wang, X. Yang, L. F. Allard, Z. Jiang, Y. Cui, J. Liu, J. Li and T. Zhang, *Nature Chem.*, 2011, **3**, 634–641.
21 M. Noǵami, R. Koike, R. Jalem, G. Kawamura, Y. Yang and Y. Sasaki, *J. Phys. Chem. Lett.*, 2010, **1**, 568–571.
22 R. Narayanan and M. A. El-Sayed, *Nano lett.*, 2004, **4**, 1343–1348.
23 T. S. Ahmadi, Z. L. Wang, T. C. Green, A. Henglein and M. A. El-Sayed, *Science*, 1996, **272**, 1924–1926.
24 L. Qu, L. Dai and E. Osawa, *J. Am. Chem. Soc.*, 2006, **128**, 5523–5532.
25 C. S. Chen, Y. T. Lai, T. C. Chen, C. H. Chen, J. F. Lee, C. W. Hsu and H. M. Kao, *Nanoscale*, 2014, **6**, 12644–12654.
26 Y. Wu, S. Cai, D. Wang, W. He and Y. Li, *J. Am. Soc. Chem.*, 2012, **134**, 8975–8981.
27 H. Berndt, A. Martin, A. Brückner, E. Schreier, D. Muller, H. Kosslick, G. U. Wolf and B. Lücke, *J. Catal.*, 2000, **191**, 384–400.
28 V. Fornés, C. López, H. H. López and A. Marťinez, *Appl. Catal. A*, 2003, **249**, 345–354.
29 M. Baltes, K. Cassiers, P. Van Der Voort, B. M. Weckhuysen, R. A. Schoonheydt and E. F. Vansant, *J. Catal.*, 2001, **197**, 160–171.
30 G. Du, S. Lim, M. Pinault, C. Wang, F. Fang, L. Pfefferle and G. L. Haller, *J. Catal.*, 2008, **253**, 74–90.
31 D. Gao, A. Zheng, X. Zhang, H. Sun, X. Dai, Y. Yang, H. Wang, Y. Qin, S. Xu and A. Duan, *Nanoscale*, 2015, **7**, 10918–10924
32 L. J. Durndell, C. M. A. Parlett, N. S. Hondow, K. Wilson and A. F. Lee, *Nanoscale*, 2013, **5**, 5412–5419.
33 H. Song, R. M. Rioux, J. D. Hoefelmeyer, R. Komor, K.Niesz, M. Grass, P. Yang and G. A. Somorjai, *J. Am. Chem. Soc.*, 2006, **128**, 3027–3037.
34 J. R. Anderson and K. C. Pratt, *Introduction to Characterization and Testing of Catalysts*; Academic Press Inc.: Orlando FL, 1985, 64.
35 F. Bernardi, M. C. M. Alves and J. Morais, *J. Phys. Chem. C*, 2010, **114**, 21434–21438.
36 B. R. Cuenya, J. R. Croy, S. Mostafa, F. Behafarid, L. Li,; Z. Zhang, J. C. Yang, Q. Wang and A. I. Frenkel, *J. Am. Chem. Soc.*, 2010, **132**, 8747–8756.
37 E. Lira, L. R. Merte, F. Behafarid, L. K. Ono, L. Zhang and B. R. Cuenya, *ACS Catal.*, 2014, **4**, 1875–1884.
38 F. Behafarid, L. K. Ono, S. Mostafa, J. R. Croy, G. Shafai, S. Hong, T. S. Rahman, S. R. Bare and B. R. Cuenya, *Phys. Chem. Chem. Phys.*, 2012, **14**, 11766–11779.
39 M. W. Small, S. I. Sanchez, N. S. Marinkovic, A. I. Frenkel and R. G. Nuzzo, *ACS Nano*, 2012, **6**, 5583–5595.
40 H. Mistry, F. Behafarid, S. R. Bare and B. R. Cuenya, *ChemCatChem*, 2014 , **6**, 348–352.
41 O. Dulaurent, X. Courtois, V. Perrichon and D. Bianchi, *J. Phys. Chem. B*, 2000, **104**, 6001–6011.
42 S. Zeradine, A. Bourane and D. Bianchi, *J. Phys. Chem. B*, 2001, **105**, 7254–7257.
43 S. Derrouiche and D. Bianchi, Langmuir, 2004, **20**, 4489–4497.
44 S. Derrouiche, V. Perrichon and D. Bianchi, *J. Phys. Chem. B*, 2003, **107**, 8588–8591.
45 S. Derrouiche, P. Gravejat and D. Bianchi, *J. Am. Chem. Soc.*, 2004, **126**, 13010–13015.
46 A. Bourane, O. Dulaurent and D. Bianchi, *Langmuir*, 2001, **17**, 5496–5502.
47 T. Chafik, O. Dulaurent, J. L. Gass and D. Bianchi, *J. Catal.*, 1993, **179**, 503–514.
48 O. Dulaurent, K. Chandes, C.Bouly and D. Bianchi, *J. Catal.*, 1999, **188**, 237–251.
49 P. Gravejat, S. Derrouiche, D. Farrussengn, K. Lombaert, C. Mirodatos and D. Bianchi, *J. Phys. Chem. C*, 2007, **111**, 9496–9503.
50 A. Bourane, M. Nawdali and D. Bianchi, *J. Phys. Chem. B*, 2002, **106**, 2665–2671.
51 O. Dulaurent and D. Bianchi, *Appl. Catal. A*, 2000, **196**, 271–280.
52 Y. Xiong and Y. Xia, *Adv. Mater.*, 2007, **19**, 3385–3391.
53 S. Mostafa, F. Behafarid, J. R. Croy, L. K. Ono, L. Li, J. C. Yang, A. I. Frenkel and B. R. Cuenya, *J. Am. Chem. Soc.*, 2010, **132**, 15714–15719.
54 H. Cheng, Y. A. Zhu, D. Chen, P. O. Åstrand, P. Li, Z. Qi and X. G. Zhou, *J. Phys. Chem. C*, 2014, **118**, 23711–23722.
55 H. Wei, X. Liu, A. Wang, L. Zhang, B. Qiao, X. Yang, Y. Huang, S. Miao, J. Liu and T. Zhang *Nat. Commun.* 2014, **5:5634** (DOI: 10.1038/ncomms6634).
56 R. A. Pollock, B. R. Walsh, J. Fry, I. T. Ghampson, Y. B. Melnichenko, H. Kaiser, R. Pynn, W. J. DeSisto, M. C. Wheeler and B. G. Frederick, *Chem. Mater.*, 2011, **23**, 3828–3840.
57 J. Lin, A. Wang, B. Qiao, X. Liu, X. Yang, X. Wang, J. Liang, J. Li, J. Liu and T. Zhang, *J. Am. Chem. Soc.*, 2013, **135**, 15314–15317.
58 S. Sun, G. Zhang, N. Gauquelin, N. Chen, J. Zhou, S. Yang, W. Chen, X. Meng, D. Geng, M. N. Banis, R. Li, S. Ye, S. Knights, G. A. Botton, T. K. Sham and X. Sun, *Sci. Rep.*, 2013, **3**, 1775.
59 G. X. Pei, X. Y. Liu, A. Wang, A. F. Lee, M. A. Isaacs, L. Li, X. Pan, X. Yang, X. Wang, Z. Tai, K. Wilson and T. Zhang, *ACS Catal.*, 2015, **5**, 3717–3725.
60 S. D. Ebbesen, B. L. Mojet and L. Lefferts, *J. Catal.*, 2007, **246**, 66–73.

61 M. J. Lundwall, S. M. McClure and D. W. Goodman, *J. Phys. Chem. C*, 2010, **114**, 7904–7912.
62 H. Song, R. M. Rioux, J. D. Hoefelmeyer, R. Komor, K. Niesz, M. Grass, P. Yang and G. A. Somorjai, *J. Am. Chem. Soc.*, 2006, **128**, 3027–3037.
63 C. Daniel, M. O. Clarté, S. P. Teh, O. Thinon, H. Provendier, A. C. Van Veen, B. J. Beccard, Y. Schuurman and C. Mirodatos, *J. Catal.*, 2010, **272**, 55–64.
64 M. Moses-DeBusk, M. Yoon, L. F. Allard, D. R. Mullins, Z. Wu, X. Yang, G. Veith, G. M. Stocks and C. K. Narula, *J. Am. Chem. Soc.*, 2013, **135**, 12634–12645.
65 P. Bazin, O. Saur, J. C. Lavalley and M. Daturi, *Phys. Chem. Chem. Phys.*, 2005, **7**, 187–194.
66 Y.T. Lai, T. C. Chen, Y. K. Lan, B. S. Chen, J. H. You, C. M. Yang, N. C. Lai, J. H. Wu, C.S. Chen, *ACS Catal.* 2014, **4**, 3824–3836.
67 A. Bourane and D. Bianchi, *J.Catal.*, 2004, **222**, 499–510.